Fermi Surface of Magnesium. II: The de Haas–van Alphen Effect*

R. W. STARK†

Department of Physics and the James Franck Institute, The University of Chicago, Chicago, Illinois

(Received 17 April 1967)

We report here the results of a detailed investigation of the de Haas–van Alphen effect in magnesium. The data were taken for the three major crystallographic planes in magnetic fields extending to 52 kG and at temperatures down to 0.31°K. The results yield cross-sectional area branches for every sheet of the single-OPW-model Fermi surface (OPW = orthogonalized plane wave). Coupled orbits generated by magnetic breakdown are shown to be responsible for many of the observed area branches. The results are in good qualitative agreement with existing models for the magnesium Fermi surface.

INTRODUCTION

THIS is the second paper of a series devoted to the experimental and theoretical determination of the electronic band structure of magnesium. The first paper[1] of this series (henceforth referred to as I) contained a brief review of the single-OPW model[2] for the magnesium Fermi surface (OPW = orthogonalized plane wave). The primary purpose of I was the presentation of the results of extensive magnetoacoustic attenuation experiments and the analysis of those results in terms of a simple two-OPW model for the band structure. This analysis yielded first-order estimates of the Fourier expansion coefficients of the local pseudopotential for magnesium. We shall assume that the reader is familiar with the contents of I and consider I to act as a sufficient introduction for the present work. In this paper we discuss some of the results of extensive investigations of the de Haas–van Alphen (DHVA) effect in magnesium.[3]

It has been known for some time that magnetic breakdown (MB) causes important changes in the DHVA effect in magnesium.[4–7] For this reason, the discussion in this paper has been somewhat separated into two parts; the first part deals with the normal DHVA effect (i.e., uninfluenced by MB), while the second part deals with the DHVA effect resulting from MB. All of these results are interpreted in terms of the Fermi-surface model presented in I.

The only previous systematic investigations of the DHVA effect which have been reported for magnesium

are those of Gordon et al.[8] and Priestley.[9] We will compare their results with ours whenever this may be pertinent and in particular whenever a point of interpretation lies open to question. In this way we hope to remove all ambiguity from the interpretation of the experimental data.

The third paper in this series (the succeeding article in this journal) will use the results contained in I and in the present paper to obtain both local and nonlocal pseudopotential models for the magnesium band structure. Quantitative comparison of the experimental data with these new models will be made in detail in that paper. For the present we will be content with qualitative comparisons of the data with the predictions of the two-OPW model; quantitative comparison of the data will be made only when it bears on the consistency of the interpretation.

EXPERIMENTAL TECHNIQUE

The DHVA effect results from the quantization of the conduction electrons's angular momentum about an applied magnetic field $\mathbf{H}$. This quantization can be observed experimentally because of the sharp cutoff in the electron distribution at the Fermi energy E_F. This cutoff leads with changing magnetic field to quantum oscillations in the diamagnetization having the general form[10]

$$\mathbf{M}(H,\theta,\varphi,T) = \sum_i \mathbf{A}_i(H,\theta,\varphi,T)$$

$$\times \sin\left[\frac{2\pi F_i(\theta,\varphi)}{H} + \beta_i(\theta,\varphi)\right], \quad (1a)$$

$$\mathbf{A}_i(H,\theta,\varphi,T) = \mathbf{C}_i(\theta,\varphi)H^{-1/2}T\left[\sinh\frac{2\pi^2 k_B T}{\hbar\omega_c}\right]^{-1}, \quad (1b)$$

where $\mathbf{A}_i(H,\theta,\varphi,T)$ and $\beta_i(\theta,\varphi)$ are the amplitude and phase, respectively, of the quantum oscillations of frequency $F_i(\theta,\varphi)$ for a given temperature T, magnetic field strength H, and magnetic field orientation (θ,φ)

[1] J. B. Ketterson and R. W. Stark, Phys. Rev. 156, 748 (1967).
[2] W. A. Harrison, Phys. Rev. 118, 1190 (1960).
[3] R. W. Stark, Bull. Am. Phys. Soc. 11, 169 (1966).
[4] M. H. Cohen and L. M. Falicov, Phys. Rev. Letters 7, 231 (1966).
[5] M. G. Priestley, L. M. Falicov, and Gideon Weisz, Phys. Rev. 131, 617 (1963).
[6] R. W. Stark, in *Proceedings of the 9th International Conference on Low Temperature Physics, Columbus, Ohio, 1964*, edited by J. G. Daunt, D. O. Edwards, F. J. Milford, and M. Yaqub (Plenum Press, Inc., New York, 1965), p. 712.
[7] R. W. Stark and L. M. Falicov, in *Progress in Low Temperature Physics*, edited by C. J. Gorter (North-Holland Publishing Company, Amsterdam, 1967), Vol. V.

[8] W. L. Gordon, A. S. Joseph, and T. G. Eck, *The Fermi Surface* (John Wiley & Sons, Inc., New York, 1960), p. 84.
[9] M. G. Priestley, Proc. Roy. Scc. (London) A276, 258 (1963).
[10] L. M. Falicov and H. Stachowiak, Phys. Rev. 147, 505 (1966).

given in polar coordinates with respect to the fundamental crystallographic axes. The frequency $F_i(\theta,\varphi)$ is related to the ith extremal cross-sectional area $\alpha_i(\theta,\varphi)$ of the Fermi surface in planes normal to $\mathbf{H}$ by the Onsager relation[11]

$$2\pi F_i(\theta,\varphi) = (\hbar c/e)\alpha_i(\theta,\varphi). \quad (2)$$

Thus, the summation in Eq. (1) is over all extremal cross sections for a given (θ,φ).

The Fermi surface of a polyvalent metal such as magnesium may have more than fifteen different extremal cross-sectional areas existing simultaneously. The size of some of these may be within a few percent of one another while others may differ by four orders of magnitude. The basic experimental problem is the spectrum analysis of Eq. (1) into each of its components. This has been done using large amplitude field-modulation techniques which will be reported in detail elsewhere.[12] However, we will attempt to outline here the basic procedures which were used.

First, the modulation frequencies f which were used were small enough so that the skin depth was always much larger than the largest dimension of the single-crystal specimen. (A typical frequency used was $f=100$ Hz). With this condition satisfied, the modulation field amplitude could be assumed to be constant throughout the entire bulk of the sample. Second, the modulation field was kept linearly polarized but could be applied in any arbitrary direction with respect to the applied dc field $\mathbf{H}$. For simplicity we will consider here only the case in which the modulation field was applied parallel to $\mathbf{H}$, i.e., only the magnitude but not the direction of $\mathbf{H}$ was changed by the modulation field. Third, the amplitude H_M of the modulation field was deliberately chosen to be large—much larger in fact than would normally be acceptable in a derivative-taking process. This was done in order to take advantage of the *nonlinear* characteristics of the DHVA oscillations. The primary effect of these nonlinearities is to generate harmonics of f.

The signal from the sample is measured using an inductively coupled pickup coil. The portion of the time-dependent output voltage of this coil that measures the DHVA effect will be of the form

$$V(t,H,\theta,\varphi,T) \propto \sum_i \sum_{n=1}^{\infty} \hat{u}\cdot A_i(H,\theta,\varphi,T)J_n\left(\frac{2\pi F_i(\theta,\varphi)H_M}{H^2}\right)$$

$$\times \sin\left[\frac{2\pi F_i(\theta,\varphi)}{H}+\beta_i(\theta,\varphi)\right]\cos2\pi nft, \quad (3)$$

where $J_n(x)$ is the Bessel function of the first kind of order n and $\hat{u}$ is a unit vector along the axis of the pickup coil. The nth harmonic component of this voltage is then phase-sensitive detected. The important point here is that the amplitudes of the various DHVA

oscillations as seen at the output of the phase-sensitive detector are no longer the inherent physical amplitudes $A_i(H,\theta,\varphi,T)$ but are those modified by the multiplicative Bessel function factor $J_n(2\pi F_i(\theta,\varphi)H_M/H^2)$. This additional factor allows one to suppress most of the DHVA frequencies in favor of one particular frequency.

For example, suppose that Eq. (1) consisted of only three components with frequencies F_i of 1×10^6 G, 2×10^6 G, and 3×10^6 G and amplitudes A_i of 1000, 10, and 1, respectively. If these were detected directly, only the 1×10^6 G frequency would be observed. However, if instead these were detected at the 12th harmonic, their relative amplitudes would depend critically on the values of H and H_M. If H is 10 kG and H_M is 225 G, an evaluation of the Bessel-function arguments[13] for each of these frequencies shows that they will be measured with relative amplitudes 1000, 7, and 0.5, respectively. If, on the other hand, H_M were changed to 89 G, the observed relative amplitudes would be 150, 1000, and 10, respectively. Finally, by setting H_M equal to 47 G, the observed relative amplitudes become 60, 160, and 1000, respectively. Thus each of these frequencies can easily be separated empirically by utilizing the nonlinear characteristics of the sample. The sample becomes in essence its own DHVA filter.

One can, in addition, utilize the dependence of $F_i(\theta,\varphi)$ on θ and φ as well as utilizing the vector character of the oscillatory magnetization[14] to obtain further discrimination between various DHVA frequencies. Also one can sweep the magnetic field such that H^{-1} varies linearly with time[15] and then use standard electronic filters at the output of the phase-sensitive detectors in order to obtain still further discrimination. All of these techniques were employed during the course of this investigation. Figure 1 shows the schematic layout of the apparatus. The details of these techniques and experimental apparatus will be discussed in Ref. 12.

In practice, one separates a given DHVA frequency F_i from all others at some (θ,φ) and then varies H in order to obtain a few hundred oscillations for an accurate calibration of $F_i(\theta,\varphi)$. Then one holds H fixed in magnitude but now varies θ or φ by rotating the sample with respect to the magnetic field (or vice versa) and obtains the change with angle in $F_i(\theta,\varphi)$ as a series of oscillations as the rotation takes place.[16] Most of the data to be presented in this paper were obtained using these rotation diagrams.

EXPERIMENTAL EXTREMAL AREAS

A composite of most of the cross-sectional areas measured during the course of this investigation is

[11] L. Onsager, Phil. Mag. 43, 1006 (1952).
[12] R. W. Stark and L. R. Windmiller (to be published).
[13] *The Annals of the Computation Laboratory of Harvard University* (Harvard University Press, Cambridge, Massachusetts, 1947), Vol. III–VII.
[14] L. R. Windmiller, Phys. Rev. 149, 472 (1966).
[15] R. W. Stark (to be published).
[16] D. Shoenberg and P. J. Stiles, Proc. Roy. Soc. (London) 281, 62 (1964).

FIG. 1. Schematic diagram of the DHVA spectrometer used to obtain the data shown in Fig. 2. The output of the oscillator is multiplied by H^2 so that the modulation amplitude

$$H_M = A H^2.$$

When this is introduced into the Bessel-function argument in Eq. (3), the argument becomes independent of H and tuning for a given DHVA frequency $F_i(\theta,\varphi)$ is accomplished by adjusting A.
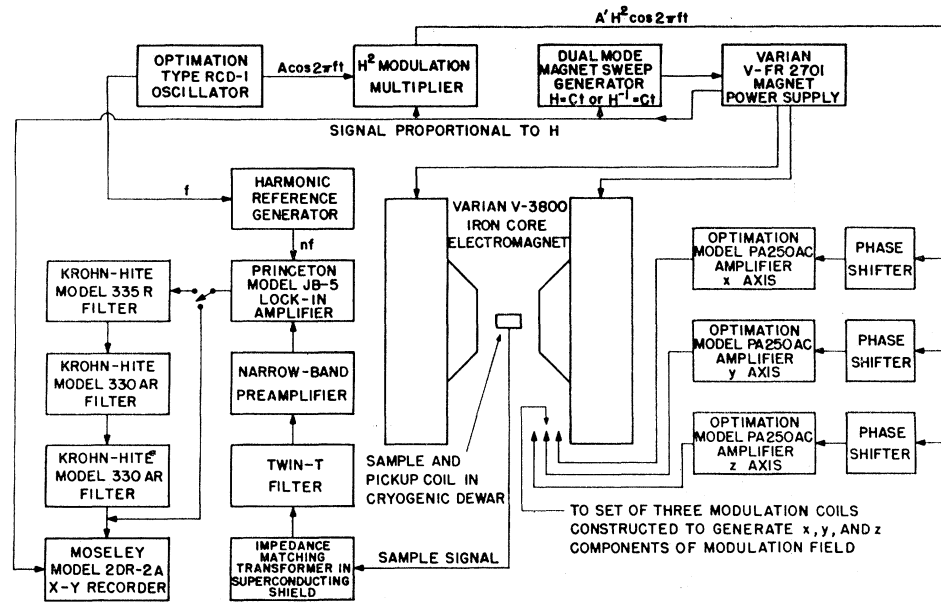
BLOCK DIAGRAM OF DHVA SPECTROMETER

shown in a semilog plot in Fig. 2. The areas are given in atomic units (a.u.), the conversion from measured experimental frequencies being made in accord with Eq. (2). The angle between [0001] and $\mathbf{H}$ in the $(10\bar{1}0)$ and $(11\bar{2}0)$ planes is measured by θ; the angle between $[10\bar{1}0]$ and $\mathbf{H}$ in the (0001) plane is measured by φ.

For simplicity we have adopted the following notation: All normal areas are designated by a Greek letter which specifies the branch of the surface upon which they originate. All areas generated by MB are designated by the first Roman letter in the name which has been assigned to the particular coupled orbit whose area is measured. Each letter carries a subscript and a superscript. The subscript signifies the major crystallographic plane in which $\mathbf{H}$ was constrained to move; 1 refers to the $(10\bar{1}0)$ plane, 2 refers to the $(11\bar{2}0)$ plane, and 3 refers to the (0001) plane. The superscript denotes the order of increasing size of the various extremal areas on a single branch of the Fermi surface. Areas assigned to the first-band cap are denoted by α, those assigned to the second-band monster are denoted by μ, those assigned to the third-band lens are denoted by λ, and those assigned to the third-band cigar are denoted by γ. The letters C and L denote extremal areas which arise when MB couples portions of the third-band butterfly and the fourth-band electron pockets. The letters T and D denote areas assigned to coupled orbits connecting the monster and cigar.

The series of extremal areas labeled by combinations of A, γ, and G without additional subscripts or superscripts are the special group of coupled orbits that are formed by a hexagonal grid of free-electron-like orbits. G, for example, is the famous "giant orbit."[4] The predicted behavior of this group has been treated in considerable detail by Falicov and Stachowiak.[10] In this

paper we will consider only the identification and assignment of some of the more prominent members of this group. The magnetic field dependence of their amplitude will be described in detail in a later communication.

All of the branches shown in Fig. 2 have been measured with an accuracy of 0.5%. The crystallographic planes were oriented in all cases to within 0.3° of the plane of rotation of H. The measurements which are represented in Fig. 2 were made in magnetic fields as high as 52 kG and at temperatures as low as 0.31°K. The assignments of these branches and the information which can be deduced from them about the Fermi surface will be discussed in detail in the next section.

Several additional frequency branches were also observed. These *are not shown* in Fig. 2 because we were able to unambiguously demonstrate that they were either harmonics of one of the branches shown or sum and difference frequencies generated by nonlinear interactions between two of the branches shown. With respect to the latter, we note that the source of the nonlinearities is uncertain; they may arise from the B–H effect or from a skin-depth modulation by the quantum oscillations in the susceptibility or by a mixing in of the de Haas–Shubnikov effect or via mutual interaction through Fermi-level oscillations or they may even be caused by a large asymmetry in the relaxation time from one orbit to another. We are not even certain at present that the source of nonlinear mixing is not strictly instrumental. Numerous tests have been made in an attempt to determine their origin but as yet these have not yielded conclusive results. In any case, these nonlinear combination branches do not yield any new information relevant to the cross-sectional areas of the Fermi surface.
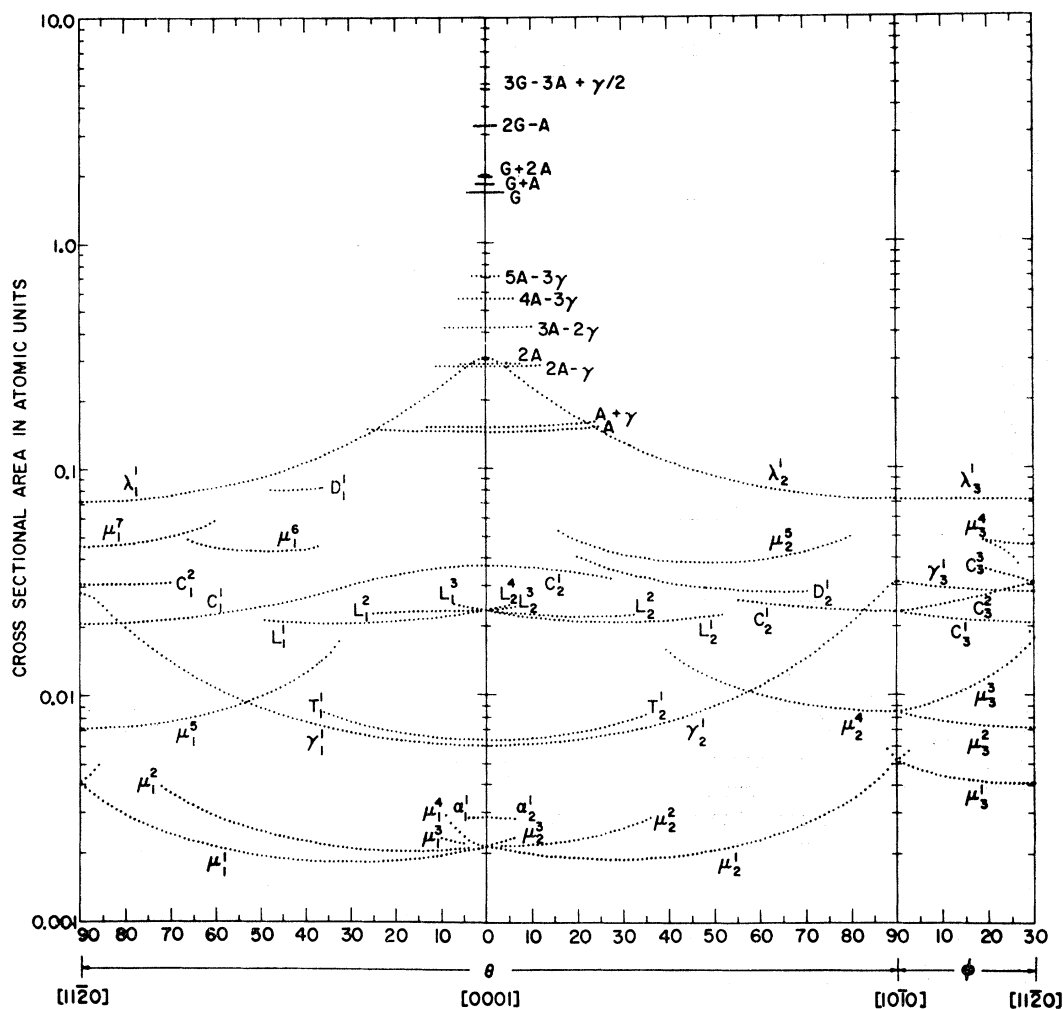
FIG. 2. A semilog plot of the DHVA cross-sectional area branches measured during this experiment. The areas are given in atomic units. Tables I and II contain listings of the areas of these branches for some directions of **H**.

DISCUSSION OF AREA ASSIGNMENTS

We will restrict our initial discussion of the area branches shown in Fig. 2 to those which are designated by Greek letters, i.e., to those which are associated with orbits existing in the limit of small magnetic fields. These will be discussed in order of their assignment to bands of increasing index.

1. The First-Band Cap

This sheet of the Fermi surface is shown in Fig. 3. The energy gap which separates the cap from the monster across the AHL plane arises solely as a result of spin-orbit coupling.[17] When **H** is in the basal plane ($\theta = 90°$), the effects of this energy gap are nearly completely eliminated by MB when $H \approx 100$ G. We note however that when **H** is parallel to [0001], the probabil-

ity for MB across this gap must go to zero since the orbiting electrons will have no component of velocity perpendicular to the AHL plane. The field $H_0(\theta)$ at which the MB probability, $P = \exp[-H_0(\theta)/H]$, is equal to $\exp(-1)$ should vary like $H_0(90°)\csc\theta$ as a function of θ. Thus one would anticipate that the DHVA
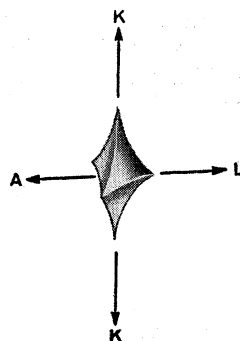

FIG. 3. The single-OPW model first-band hole pocket (the "cap"). This is centered on the symmetry point H of the hexagonal Brillouin zone.

---

[17] L. M. Falicov and M. H. Cohen, Phys. Rev. **130**, 92 (1963).

oscillations arising from orbits around the cap will have an observable amplitude only for very small values of θ.

The α_1^1 and α_2^2 area branches shown in Fig. 2 have been assigned to the cap. The size of these branches is compatible with that predicted by the two-OPW model described in I. They were observable only within 6° of [0001]. The DHVA oscillations for these branches existed in fields as low as 1.2 kG. As H was increased, their amplitude decreased rapidly relative to the smallest set of μ branches. The α branches could not be observed for fields above 3.1 kG. All of these features are compatible with the assignment of the α branches to the cap. This assignment should be considered to be reasonable but not necessarily unambiguous. At $\theta=0°$, the α branches have an area of 3.2×10^{-3} a.u. These branches are the least accurately determined of all of the area branches shown in Fig. 2.

2. The Second-Band Monster

This sheet of the Fermi surface consists in essence of a multiply connected set of two types of intersecting hyperbolic necks. The model discussed in I predicts the existence of several extremal areas on the monster. Some of these are shown in Fig. 4 for H in the $(10\bar{1}0)$ plane at $\theta\approx65°$,

All of the branches labeled by μ in Fig. 2 have been assigned to the monster. The set which has the smallest area, μ_1^1, μ_1^2, μ_1^3, μ_1^4, μ_2^1, μ_2^2, μ_2^3, and μ_3^1, has been assigned to the diagonal arms of the monster. This assignment is in accord with that given earlier by Gordon et al.[8] There is no significant discrepancy between our data and theirs; the angular variation of these branches indicate that they arise from sheets of the surface that have the topology of hyperbolic necks whose axes are tilted about 28.7° from the ΓA zone line in the ΓKHA-zone planes. The symmetry of the data indicates a set of at least six of these necks. The only possible assignment of these areas to the Fermi-surface
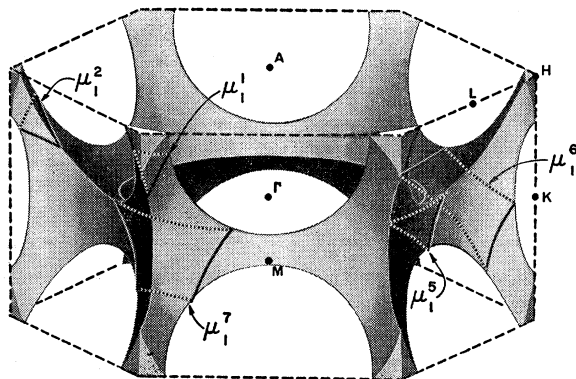

FIG. 4. The single-OPW model second-band hole sheet (the "monster"). Several orbits are shown on the surface for H tilted approximately 65° from [0001] toward [11$\bar{2}$0], i.e., from ΓA toward ΓK. These orbits are labeled with the symbol assigned to the corresponding area branches in Fig. 2.
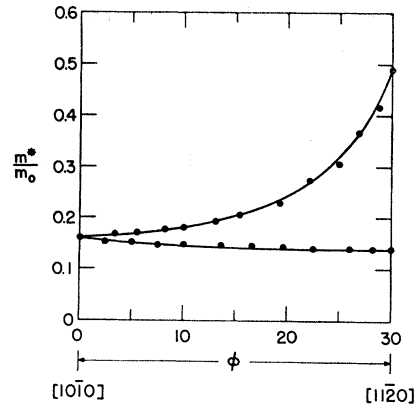

FIG. 5. The effective cyclotron mass m^* for the μ_3^2 and μ_3^3 area branches in Fig. 2. The data were obtained from the variation with temperature of the DHVA amplitude for these branches.

model discussed in I is to the diagonal arms of the monster. The μ_1^1 and μ_1^2 orbits of this group are shown on the monster in Fig. 4.

Definite saddle-point cutoffs were observed in μ_1^2 at $\theta=72°$ and in μ_2^2 at $\theta=36°$. μ_1^1 and μ_2^1 were followed 4° and 2°, respectively, past $\theta=90°$ but it was not possible to ascertain whether either cut off at these points. μ_3^1 connects μ_1^1 and μ_2^1 across the basal plane. The angular range over which these branches were observed is considerably larger than that predicted by the single-OPW model but is in better agreement with the predictions of the two-OPW model.

The μ_1^5, μ_2^4, μ_3^2, and μ_3^3 branches have been assigned to the monster waist. These branches have been followed over part of their range by both Gordon et al.[8] and Priestley.[9] There is no basic discrepancy in the areas measured in their experiments and ours. This group of area branches has minimum area for H along [11$\bar{2}$0]. μ_1^5 increases as expected for a hyperbolic neck as θ decreases until it appears to cut off at $\theta=32.5°$. μ_2^4 also increases hyperbolically as θ decreases and appears to cut off at $\theta=39.5°$. μ_3^2 joins μ_1^5 with μ_2^4 across the basal plane and μ_3^3 extends to 1° beyond [11$\bar{2}$0], at which point it could no longer be followed. The symmetry and angular variations of these branches unambiguously assigns them to the monster waist. Typical orbits of this group are shown in Fig. 4.

The effective cyclotron mass m^* for the μ_3^2 and μ_3^3 branches was determined from the variation with temperature of their respective DHVA amplitudes. A plot of m^* in units of the free-electron mass m_0 is shown in Fig. 5 for these branches. The minimum value of $m^*=0.138\pm0.004$ occurs on μ_3^2 for H parallel to [11$\bar{2}$0], the value for H parallel to [10$\bar{1}$0] is $m^*=0.162$ ±0.004, and the value for μ_3^3 when H is parallel to [11$\bar{2}$0] is $m^*=0.48\pm0.03$.

The μ_1^6 and μ_2^5 branches have been assigned to orbits about the intersection of two diagonal arms of the monster with the monster waist. The range in θ

over which both of these branches were obtained appears to be limited by the fact that their signals gradually diminished to the noise level. We do not believe that the limits shown in Fig. 2 represent cutoffs. Measurements of m^* for $\mu_2{}^5$ showed that this was approaching 0.5 at the measured ends of the branch. Thus it is probable that we lost this branch as a result of spin-splitting of the Landau levels and not as a result of a saddle-point cutoff. Typical orbits associated with the $\mu_1{}^6$ branch are shown on the monster in Fig. 4. The assignment of these branches is made quite unambiguous by the existence of the $D_1{}^1$ and $D_2{}^1$ branches. The assignment of these will be discussed later.

The $\mu_1{}^7$ and $\mu_3{}^4$ branches have been assigned to another orbit about the junction of the diagonal arms of the monster and the monster waist. A typical orbit is shown in Fig. 4. $\mu_1{}^7$ appears to cut off at $\theta = 60°$. $\mu_3{}^4$ appears to cut off at $\varphi = 18.5°$, near which it also splits into two separate branches. This splitting is consistent with the two-OPW model discussed in I. $\mu_1{}^7$ should be a maximum area. The upper branch of $\mu_3{}^4$ should also be a maximum area. However, shortly after the minimum waist area $\mu_3{}^3$ cuts off, a new minimum area appears which corresponds to the lower branch of $\mu_3{}^4$. The two branches then apparently coalesce before $\mu_3{}^4$ cuts off.

Priestley[9] obtained some data for the $\mu_1{}^7$ branch but split it into two branches which he labeled C' and M. His assignment of these is incorrect. It should be also noted that he assigned the branch which he labeled F to the $\mu_1{}^7$ orbit shown in Fig. 4. His branch F is in reality not the fundamental but is instead the second harmonic of the $\mu_1{}^7$ branch.

3. The Third-Band Cigar

None of the previously published data relevant to the cigar has been complete enough to allow a systematic comparison with any Fermi-surface model. Gordon et al.[8] obtained data which agree quite well with the branches which we have labeled $\gamma_1{}^1$ and $\gamma_2{}^1$. Although their data were limited to the angular range $\theta \lesssim 55°$, they were able to deduce from the size and variation with θ of the portion of the γ branches which they obtained that these arose on the cigar. This assignment is confirmed by the complete set of data for these branches shown replotted in Fig. 6. Also shown in Fig. 6 for comparison is the area of the single-OPW cigar. The $\gamma_3{}^1$ branch joins $\gamma_2{}^1$ with $\gamma_1{}^1$ in the (0001) plane. The comparison of the measured and calculated branches indicate that the geometry of the cigar is very similar to the single-OPW model cigar but that it is somewhat larger and more elongated. Its small cross section is nearly that of an equilateral triangle. The corners of the triangle must be only slightly rounded by the very weak (10$\bar{1}$0) energy gap. The enlargement and elongation presumably results from a lowering of this energy band
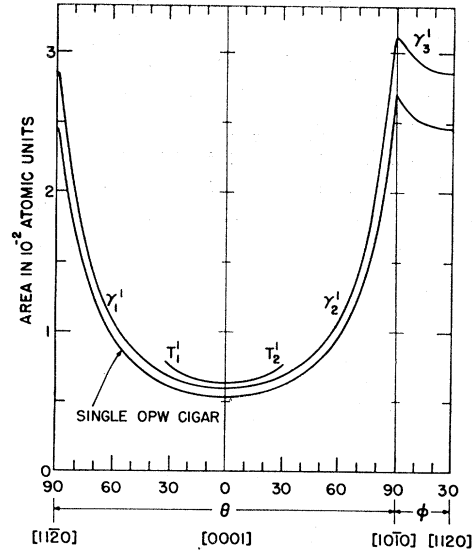

FIG. 6. The $\gamma_1{}^1$, $\gamma_2{}^1$, and $\gamma_3{}^1$ DHVA area branches arise from the third-band cigar. Shown for comparison are the branches that would arise from the single-OPW cigar. Also shown are the $T_1{}^1$ and $T_1{}^2$ area branches; these have been assigned to the trifoliate orbit shown in Fig. 10.

(relative to the nearly free electron band) in the region of the Brillouin zone along the KH line by the fairly large Fourier component of the pseudopotential associated with the (10$\bar{1}$1)-type zone planes.

That the tip of the cigar is as nearly sharp and pointed along KH as the single-OPW cigar is readily deduced from the fact that the inflection point in the $\gamma_2{}^1$ branch occurs within $1.3°$ of [10$\bar{1}$0]. When $\mathbf{H}$ is parallel to [10$\bar{1}$0], symmetry requires that the extremal orbit lie in the ΓKHA zone plane. For all other directions of $\mathbf{H}$ in the basal plane ($\varphi \neq 0°$) the extremal orbit will not include the KH line since the cigar has only threefold symmetry about KH. As seen in Fig. 6 the variation with angle of the γ branches follow very closely the variation expected for the single-OPW model, although they are a bit larger in magnitude. From this it appears that the energy gap across the (10$\bar{1}$0)-zone planes must be quite small in the region not only around K but along the entire length of the KH line.

Priestley[9] reported data for the cigar but his cross-sectional areas are somewhat larger than the γ branches; it seems that his data represent an average of the γ branches and those labeled $T_1{}^1$ and $T_1{}^2$ in Fig. 2. This is not surprising, since the amplitude of the DHVA oscillations associated with the T branches was larger than that of the γ branches for $H \gtrsim 15$ kG. The value of the effective cyclotron mass which Priestley measured for his branch when $\mathbf{H}$ was parallel to [0001] was $0.22m_0$. This again is about the average value of the masses for the γ branch ($0.10m_0$) and the T branch ($0.34m_0$) which we measured for this orientation of $\mathbf{H}$.

4. The Third-Band Lens

The area branches labeled λ_1^1, λ_2^1, and λ_3^1 in Fig. 2 have been assigned to the lens. λ_3^1 is nearly constant, varying by less than 0.15% over the basal plane. The λ_1^1 and λ_2^1 branches are nearly identical functions of θ; the lens appears to be very nearly a surface of revolution about the ΓA zone line. This is in accord with the magnetoacoustic results for the lens reported in I.

The area-inversion scheme proposed by Mueller[18] was used to transform the λ branches into equivalent Fermi surface radii for the lens. The result of this inversion is shown in Fig. 7. The solid contour is the locus of the radii in the ΓMLA plane obtained by inversion of the DHVA area branches. The dashed contour is the cross section of the single-OPW model lens. Shown for comparison are the magnetoacoustic calipers reported in I. The agreement between these two sets of empirical radii is quite good.

It should be pointed out that the inversion of the lens data was not accomplished directly.[19] The large curvature of the lens as it crosses the ΓKH plane led to a poorly covergent expansion in spherical harmonics. A coordinate transformation was first made on the λ branches to make them as nearly constant as possible, i.e., the lens was transformed into a pseudosphere. These transformed area branches were then inverted into radii and the inverse coordinate transformation applied to the radii to regain the actual lens radii. The final agreement between the inverted radii and the magnetoacoustic calipers gives one a measure of confidence in the application of Mueller's inversion scheme.[18]

Priestley[9] observed area branches which he assigned to the lens. His data agree reasonably well with the λ_1^1 and λ_2^1 branches for $\theta \gtrsim 25°$. However, for $\theta \lesssim 25°$, it appears that he lost the λ_1^1 and λ_2^1 branches and followed instead the separate branch which we have labeled A in Fig. 2. The misidentification of A led to erroneous estimates for the lens Fermi surface radii, making the lens appear to be seriously distorted from the single-OPW model.

5. The Third-Band Butterflies and Fourth-Band Electron Pockets

At this point we must begin considering the effects of coupled orbits generated by MB. The reason for this is that the energy gap which separates the third and fourth bands across the AHL plane results solely from spin-orbit interactions; this gap is very small over the entire plane and vanishes along the AL zone line. Thus, DHVA frequencies associated with these two sheets of the Fermi surface will most likely arise from orbits coupled via MB to both sheets. Fig. 8(a) shows the cross sections of the butterfly and fourth-band electron
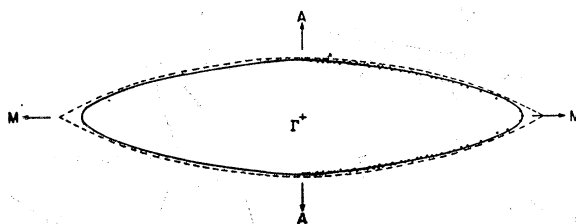
[18] F. M. Mueller, Phys. Rev. 148, 636 (1966).
[19] J. C. Kimball and F. M. Mueller (to be published).

FIG. 7. Cross section of the third-band lens in the ΓMA plane of the Brillouin zone. The dashed contour is for the single-OPW model. The solid curve results from the inversion of the λ_1^1, λ_2^1, and λ_3^1 area branches into $\mathbf{k}$ vectors. Shown for comparison are the magnetoacoustic calipers reported in I.

pocket in the $ALM\Gamma$ plane of the Brillouin zone. If the energy discontinuity between these two sheets were finite along the AL line, these contours would be the extremal orbits. However, the discontinuity vanishes along the AL line and is sufficiently small away from the AL line in the ALH plane that MB will recouple the orbit segments to form the type of orbits shown in Fig. 8(b). The geometry of the surface sheets will appear not as the butterfly [Fig. 8(d)] and the fourth-band electron pocket [Fig. 8(e)] but as the clam-shaped combination sheet [Fig. 8(f)].

The C_1^1, C_1^2, C_2^1, C_3^1, C_3^2, and C_3^3 branches shown in Fig. 2 have been assigned to extremal orbits on this clam. There was definite evidence of a second branch splitting from both C_1^1 and C_2^1 at $\theta = 0°$ but neither of these branches could be followed for any distance. The branch splitting from C_1^1 should join with C_1^2. The measured effective cyclotron mass of the degenerate C branches at $\theta = 0°$ was $0.49 \pm 0.02 m_0$. This mass decreases slowly as θ increases on both C_1^1 and C_2^1 but might well increase slightly to $0.5 m_0$ on the missing two branches and hence eliminate the fundamental DHVA signal for these. In any event, the portion of the complete set of branches which have been measured is sufficient to identify their source as the clam-shaped combination surface. These branches have minimum area for H parallel [$11\bar{2}0$]. For this orientation, the extremal orbit has the shape shown in Fig. 8(b). The area of these branches agrees reasonably well with the predictions of the two-OPW model given in I.

We will now consider further complications of the butterfly-fourth-band electron-pocket complex. MB across the (0001) zone plane led to the clam-shaped structure discussed above. Notice in Fig. 8(a) that the other line of degeneracy between these third-band and fourth-band sheets of the single-OPW model Fermi surface occurs in the ($10\bar{1}0$)-zone plane. An estimate of the effective local pseudopotential coefficient for this plane was given in I based on MB data between the monster and cigar near K. Its value of approximately 5×10^{-4} Ry is so small that MB near K is important in fields as small as 2 kG. The following paper shows that the actual [$10\bar{1}0$] pseudopotential coefficient is about an order of magnitude larger but that second-order
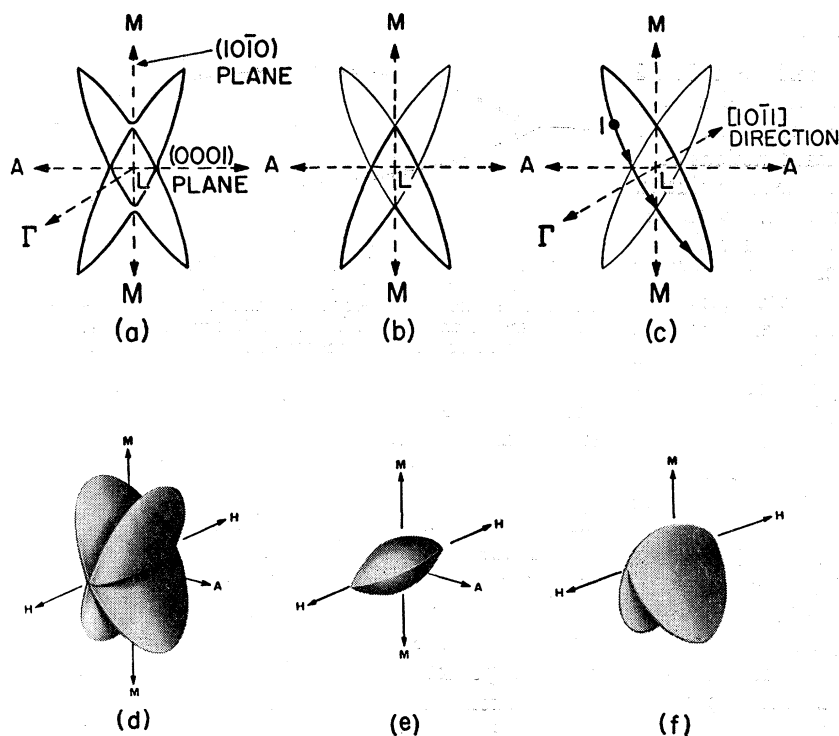
FIG. 8. The third-band butterfly and fourth-band electron pocket: (a) single-OPW cross section of each in the ALM plane; (b) single-OPW cross section in the ALM plane of the clam generated when MB recouples the orbit segments of (a); (c) single-OPW cross section in the ALM plane of the [$10\bar{1}1$] lens generated when MB further recouples the orbit segments of (a); (d) the single-OPW model butterfly; (e) the single-OPW model fourth-band electron pocket; (f) the single-OPW model clam.

corrections, primarily from the [$10\bar{1}1$] pseudopotential coefficient, reduce the [$10\bar{1}0$] energy gap to this small value near K. The [$10\bar{1}0$] energy gap between the butterfly and the fourth-band electron pocket must vanish in the immediate vicinity of the ALH-zone plane, since symmetry requires that the two bands be degenerate in this plane (with the exception of the spin-orbit coupling induced gap). The [$10\bar{1}0$] gap will increase rapidly as one goes away from this plane but will remain small enough to undergo MB at modest field strengths for a reasonable distance above and below the ALH plane. For the sake of argument, we will assume that the [$10\bar{1}0$] gap remains small over the entire ($10\bar{1}0$) plane. In other words, MB of the energy gap between the butterfly and fourth-band electron pocket in the ($10\bar{1}0$) plane will be assumed. Thus, an electron orbiting on this surface for H parallel to [$11\bar{2}0$] would be expected to follow the trajectory shown in Fig. 8(c).

Starting at point "1" on the butterfly, it would first tunnel through the spin-orbit gap across the (0001) plane to the fourth band, traverse that and then tunnel across the small [$10\bar{1}0$] gap onto the adjacent butterfly wing, traverse that and continuing this behavior would ultimately arrive back at point 1. Orbits made up in this way would appear to arise on a sheet of the surface having the geometry of a convex lens centered on the ($10\bar{1}1$)-zone faces.

The area branches labeled $L_1{}^1$, $L_1{}^2$, $L_1{}^3$, $L_2{}^1$, $L_2{}^2$, $L_2{}^3$, and $L_2{}^4$ shown in Fig. 2 have been assigned to this simple surface of complex origin. The variation with θ

and the total number of branches observed require that these branches arise on a surface centered in the ($10\bar{1}1$) zone planes. Their variation with θ agrees with that expected for lenses centered on the ($10\bar{1}1$) planes. In addition, these lenses should be very nearly surfaces of revolution about the ΓL zone line. It is obvious that the area shown in Fig. 8(b) is exactly the same as the area shown in Fig. 8(c) and the area shown in Fig. 8(c) is the minimum area of this lens if it is a surface of revolution about ΓL. The minimum area of the $L_2{}^1$ branch is 0.0208 a.u. This compares very well with the minimum area of the $C_1{}^1$ branch which also is 0.0208 a.u. Thus the assignments of the C and L branches are internally self-consistent. None of the L branches could be followed for $\theta \gtrsim 45°$. This indicates that the [$10\bar{1}0$] energy gap must grow quite rapidly as one goes out of the AHL plane.

6. Orbits Coupled by MB between the Monster and Cigar

The $T_1{}^1$ and $T_2{}^1$ area branches shown in Fig. 2 have been assigned to a trifoliate shaped orbit which is generated when MB couples the diagonal arms of the monster to the tip of the cigar. The first pertinent point that we should note about these branches is that they are essentially symmetric about [0001]. There was no evidence that any other branches split from these at [0001], so that they must arise from an orbit which has a minimum of threefold symmetry when H is parallel to [0001]. Thus either the KH or ΓA zone line
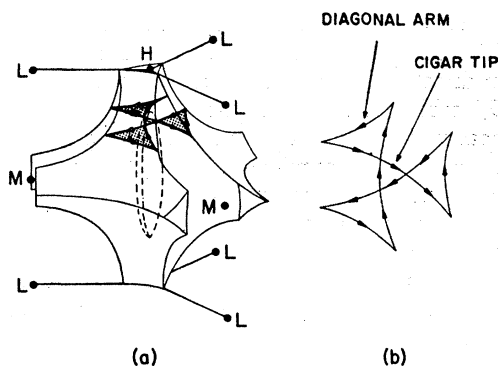
FIG. 9. (a) Portion of the second-band monster in the repeated zone scheme showing the trifoliate orbit which is generated when MB couples the diagonal arms of the monster to the cigar. The cigar outline is shown by the dashed lines. This orbit gives rise to the $T_1{}^1$ and $T_2{}^1$ area branches shown in Fig. 2 and in Fig. 7; (b) projection of this orbit on the ΓKM plane.

is the appropriate center line of symmetry for the piece or pieces of the Fermi surface which give rise to these branches. In addition, the rate of increase of area with increasing θ is that which would be expected for a hyperbolic neck. The only portion of our Fermi-surface model capable of generating these branches in the absence of MB is the junction of the diagonal arms of the monster with the AHL plane around the point H. There are, however, several reasons for not assigning the $T_1{}^1$ and $T_1{}^2$ branches to this arm junction.

First, when **H** is parallel to [0001] the arm junction should have an area that is only a few percent larger than the cap. As can be seen in Fig. 2, the T branches are more than twice as large as the α branches which have been assigned to the cap. Second, the T branches have an effective cyclotron mass of $m^* = 0.340 \pm 0.005$ m_0 for **H** parallel to [0001]. This is about three times larger than expected for the arm junction. Finally and *conclusively*, the DHVA oscillations for these branches had an amplitude dependence as a function of H which did not satisfy the theoretical amplitude expression given in Eq. (1); the amplitude was much too small at low fields. An amplitude correction factor involving tunnelling at six MB junctions was required to bring the
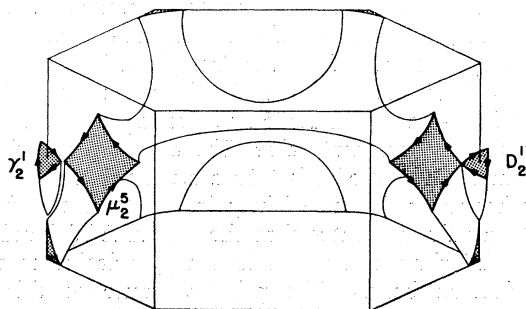

FIG. 10. Portions of the monster and cigar showing the $\gamma_2{}^1$, $\mu_2{}^5$, and $D_2{}^1$ orbits. The $D_2{}^1$ orbit is generated when MB couples the $\gamma_2{}^1$ and $\mu_2{}^5$ orbits. These orbits are drawn for $\theta \approx 45°$.

magnetic field dependence of the experimental amplitude into agreement with the theoretical expression.

Thus, since we know that MB occurs between the monster and the cigar and that the amplitude of these DHVA oscillations requires correction for six MB junctions, it is natural to assign these branches to the trifoliate orbit shown in Fig. 9(a) and 9(b). In this connection, we note that the area of the T branches at $\theta = 0°$ is 6.34×10^{-3} a.u. The area of the diagonal arms is 2.15×10^{-3} a.u. Three of these making up the lobes of the trifoliate orbit would have an area of 6.45×10^{-3} a.u. To get the total quantized area, we must subtract the area of the small triangle corresponding to the orbit around the tip of the cigar. Thus the small difference between these two areas can easily be accounted for.
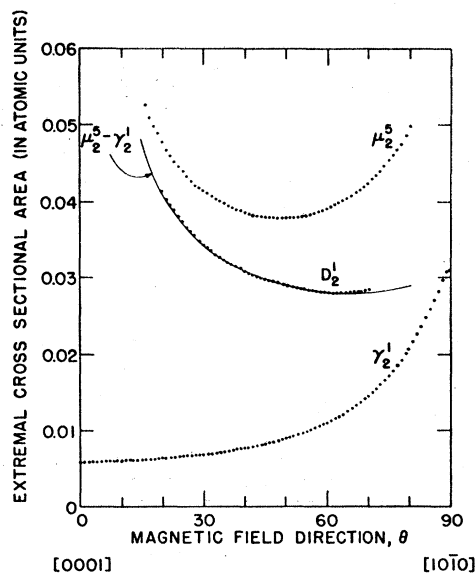

FIG. 11. The $\gamma_2{}^1$, $\mu_2{}^5$, and $D_2{}^1$ area branches. The solid curve is the difference $\mu_2{}^5(\theta) - \gamma_2{}^1(\theta)$. The agreement of the $D_2{}^1$ branch with the solid curve verifies the MB origin of the $D_2{}^1$ branch.

In addition, the effective mass for the trifoliate orbit $(0.34m_0)$ is slightly larger than three times the effective mass for the diagonal arms $(0.11m_0)$ as expected for this assignment.

Another area branch which results when MB couples orbits on the monster and the cigar is labeled $D_2{}^1$ in Fig. 2. This is given directly by the difference between the $\mu_2{}^5$ and the $\gamma_2{}^1$ branches. All of these areas are shown on the monster in Fig. 10 for $\theta = 45°$. Note that in this particular case, the ΓK zone line is the line of symmetry for both the $\mu_2{}^5$ and $\gamma_2{}^1$ orbits, and hence is also the line of symmetry for the coupled $D_2{}^1$ orbit. Figure 11 shows a replot of all three area branches on a linear scale. The solid curve is the difference $\mu_2{}^5(\theta)$ $- \gamma_2{}^1(\theta)$. The agreement between the predicted area for the coupled orbit and the data for all values of θ confirms both the generation of the $D_2{}^1$ branch by MB and our original assignment of the $\mu_2{}^5$ branch to the
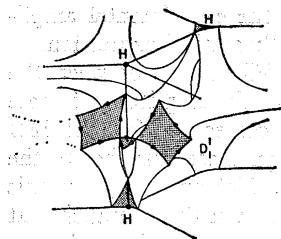
FIG. 12. A portion of the monster and cigar in the extended zone scheme showing a typical D_2^1 orbit which is generated when MB couples two adjacent monster orbits across the cigar. These orbits are drawn for $\theta \simeq 45°$.

particular orbit on the monster, which is shown in Fig. 10. Note that this orbit can exist only in the intermediate regime of MB where the breakdown probability is $0 < P < 1$, since it requires two incidents of tunnelling in getting onto and off of the cigar and two incidents of Bragg reflection to complete the orbit around the cigar.

The analog of the D_2^1 branch in the $(10\bar{1}0)$ plane is the D_1^1 branch. However, in this case the extremal orbit for the μ_1^6 branch does not lie in the same plane in $\mathbf{k}$ space as the extremal orbit for the γ_1^1 branch. Thus, the coupled orbit will not have an area given by strict algebraic combinations of μ_1^6 and γ_1^1, although the extremal planes do lie close enough together that one would expect approximate agreement with the algebraic combination.[6] The D_1^1 branch requires coupling of two μ_1^6 orbits across a γ_1^1 orbit as shown in Fig. 12 so that its approximate area is given by $2\mu_1^6 - \gamma_1^1$. At $\theta = 45°$, the D_1^1 branch has an area of 8.06×10^{-2} a.u. compared with the algebraic combination of 7.84×10^{-2} a.u.; at $\theta = 40°$, the D_1^1 branch has an area of 8.13×10^{-2} a.u.

TABLE I. DHVA areas and cyclotron masses at symmetry directions and branch extrema.

Branch symbol	θ	Area (in a.u.)	m^* (in units of m_0)
μ_1^1	0°	2.15×10^{-3}	0.11 ± 0.01
μ_1^1	28.7°	1.83×10^{-3}	0.10 ± 0.01
μ_1^1	90°	4.09×10^{-3}	...
μ_1^2	23°	2.05×10^{-3}	...
μ_2^1	26.8°	1.91×10^{-3}	...
μ_2^1	90°	5.12×10^{-3}	...
α_1^1	0°	3.15×10^{-3}	...
γ_1^1	0°	5.98×10^{-3}	0.100 ± 0.002
γ_1^1	90°	2.87×10^{-2}	0.38 ± 0.03
γ_2^1	90°	3.13×10^{-2}	...
T_1^1	0°	6.34×10^{-3}	0.340 ± 0.005
μ_1^5	90°	7.21×10^{-3}	0.138 ± 0.004
μ_2^4	90°	8.45×10^{-3}	0.162 ± 0.004
μ_3^3	$\varphi = 30°$	1.77×10^{-2}	0.48 ± 0.03
L_1^1	0°	2.34×10^{-2}	0.34 ± 0.02
L_1^1	31.7°	2.07×10^{-2}	...
L_2^1	26.8°	2.08×10^{-2}	0.32 ± 0.01
L_2^2	19.1°	2.19×10^{-2}	...
C_1^1	0°	3.72×10^{-2}	0.49 ± 0.02
C_1^1	90°	2.08×10^{-2}	0.32 ± 0.01
C_2^1	90°	2.31×10^{-2}	...
C_3^2	$\varphi = 30°$	3.12×10^{-2}	...
μ_1^6	46.6°	4.33×10^{-2}	...
μ_1^7	90°	4.57×10^{-2}	0.45 ± 0.03
μ_2^5	48.5°	3.80×10^{-2}	0.33 ± 0.01
D_1^1	45.4°	8.06×10^{-2}	...
λ_1^1	0°	30.8×10^{-2}	...
λ_1^1	90°	7.27×10^{-2}	0.42 ± 0.01
λ_2^1	90°	7.26×10^{-2}	0.42 ± 0.01

compared with the algebraic combination of 7.90×10^{-2} a.u. The deviation of the experimental area is in the proper direction from the approximate prediction, since the D_1^1 orbit must lie in a plane located between the extremal plane for μ_1^6 and the extremal plane for γ_1^1 because μ_1^6 is a minimum area and γ_1^1 is a maximum area on their appropriate sheets of the Fermi surface. Thus, in the D_1^1 extremal plane the nonextremal μ_1^6 orbit will enclose an area slightly larger than the extremal μ_1^6 area branch and the nonextremal γ_1^1 orbit will enclose an area slightly smaller than the extremal γ_1^1 area branch.

Some of the cross-sectional areas for all of the major area branches shown in Fig. 2 are tabulated in Table I. Most of these are values for H parallel to one of the three major crystallographic axes. Some are the areas at extremums on given branches. Also included in Table I are the measured values of m^*.

## 7. The Hexagonal Grid of Coupled Free-Electron-Like Orbits

When H is parallel to $[0001]$, MB between the monster and the cigars in the ΓKM plane generates the hexagonal grid of coupled orbits shown in Fig. 13. This case has been treated in detail theoretically by Falicov and Stachowiak.[10] All of the remaining area branches shown in Fig. 2 have been assigned to various orbits in this network.

The small triangular orbit γ is the extremal orbit about the cigar. This is the γ branch at $\theta = 0°$ in Fig. 2. Its area is 5.98×10^{-3} a.u. The lens shaped orbit A results in the intermediate regime of MB and requires four incidents of tunnelling and two of Bragg reflection. The branch A in Fig. 2 has been assigned to this orbit; its area is 0.144 a.u. The free-electron-like or "giant-orbit" G results when the electron tunnels at all twelve MB junctions on its circuit. The branch G in Fig. 2 has been assigned to this orbit. It has an area of 1.67 a.u. It was the observation of the G branch in Priestley's[9] earlier experiment that led Cohen and Falicov[4] to postulate the existence of MB.

A check on the consistency of these assignments can be obtained by noting that symmetry requires that $G = B + 3A - 2\gamma$, where B is the cross-sectional area of the ΓKM plane of the Brillouin zone. This area, which is readily calculated from the data given in Table I of I, is $B = 1.255$ a.u. The value of G given by the combination of B, A, and T is 1.676 a.u. This agrees quite well with the experimental value. The area expected from the single-OPW model is 1.66 a.u.; the fact that the experimental value is slightly larger than the free-electron value indicates that the second $E(\mathbf{k})$ band in the ΓKH plane is lowered in energy relative to the free-electron bands. The primary cause of this is probably the fairly large $[10\bar{1}1]$ coefficient of the pseudopotential.

The G branch terminates at $\theta = 4.2°$ in both the $(10\bar{1}0)$

FIG. 13. Hexagonal grid of free-electron-like coupled orbits generated by MB between the second-band monster and the third-band cigar in the ΓKM plane for $\theta=0^\circ$. Various orbits for which the corresponding DHVA frequencies have been observed are shown on the grid. The observed and predicted areas are listed in Table II.
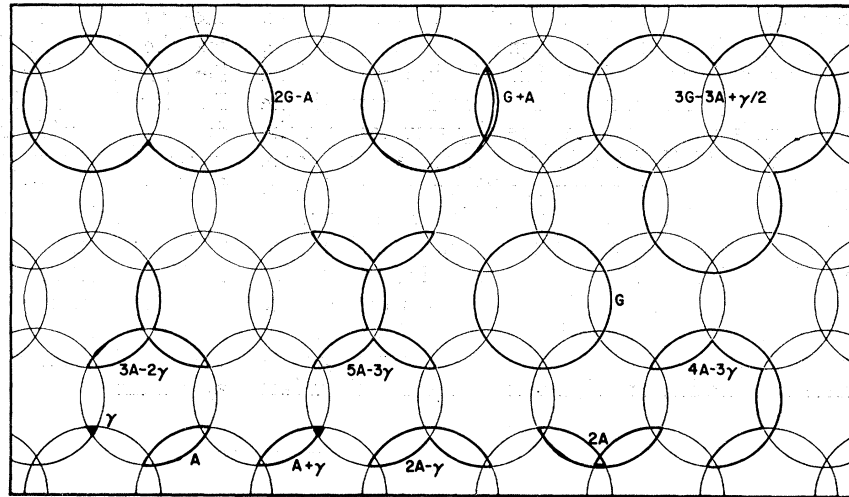
and $(11\bar{2}0)$ planes. This agrees quite well with earlier measurements.[5,20] Since this range is limited by the height of the monster waist measured parallel to ΓA in the ΓMLA plane of the Brillouin zone, we can use the magnetoacoustic measurements of the waist reported in I to predict this range. The predicted value of 4.3° adds additional confirmation of the consistency that exists between these two experiments.

The effective cyclotron masses were determined from the variation with temperature of the DHVA oscillations of the γ, A, and G orbits at $\theta=0^\circ$. The values obtained for these in units of the free-electron mass are $m_\gamma^*=0.100\pm0.002$, $m_A^*=0.55\pm0.02$, and $m_G^*=1.40 \pm0.05$, respectively. Since the orbit G is made up of segments of the γ and A orbits, m_G^* must be related to m_γ^* and m_A^* by $m_G^*=3m_A^*-2m_\gamma^*$. This yields a value of 1.45 ± 0.06 for m_G^*, which is within the experimental error of the measured value.

All of the remaining branches which are shown in Fig. 2 have been assigned to other orbits which are

TABLE II. DHVA areas for coupled orbits shown in Fig. 13.

Orbit symbol	Experimental area (in a.u.)	Area predicted by combination of A, γ, and G
γ	5.98×10^{-3}	$\cdots$
A	1.44×10^{-1}	$\cdots$
$A+\gamma$	1.50×10^{-1}	1.50×10^{-1}
$2A-\gamma$	2.82×10^{-1}	2.82×10^{-1}
$2A$	2.88×10^{-1}	2.88×10^{-1}
$3A-2\gamma$	4.21×10^{-1}	4.20×10^{-1}
$4A-3\gamma$	5.60×10^{-1}	5.58×10^{-1}
$5A-3\gamma$	7.00×10^{-1}	7.02×10^{-1}
G	1.67	$\cdots$
$G+A$	1.81	1.814
$G+2A$	1.96	1.958
$2G-A$	3.20	3.196
$3G-3A+\gamma/2$	4.60	4.575

[20] R. W. Stark, T. G. Eck, and W. L. Gordon, Phys. Rev. 133, A443 (1964).

generated in the hexagonal grid of coupled orbits by MB in the intermediate regime. These orbits, which are shown in Fig. 13, have been labeled with the same symbol as that given to the area branch in Fig. 2. The observed areas of all of these coupled orbits are tabulated in Table II together with the areas predicted for them by the appropriate combinations of γ, A, and G.

A complete discussion of the spectrum of DHVA oscillations arising from this coupled orbit network will be the subject of another paper. This will include the data concerning the relative amplitudes of all these orbits as a function of magnetic field strength and a detailed comparison of these amplitudes with the predictions of theory.

CONCLUSIONS

DHVA area branches have been obtained for every sheet of nearly-free-electron Fermi surface. At each point on these area branches we sample, in reality, a continuous set of $\mathbf{k}$ vectors from some center point on the orbit to the Fermi surface; the integral of these around the orbit gives the area. We note then, that a complete area branch taken over a range in θ or φ carries information not only about the cross section of the Fermi surface but of solid angles of $\mathbf{k}$ vectors to the Fermi surface as well. The fundamental problem involved in making use of the DHVA data to determine the $E(\mathbf{k})$ bands for the metal is that of converting the DHVA area branches into $\mathbf{k}$ vectors at the Fermi surface.

If the sheet of the Fermi surface giving rise to a particular area branch has simply connected closed topology with inversion symmetry then an area inversion scheme such as that proposed by Mueller[18] allows a direct conversion of area into $\mathbf{k}$ vectors. The only sheet of the magnesium Fermi surface satisfying these criteria is the third-band lens. The area branches for this sheet of the Fermi surface were inverted into $\mathbf{k}$ vectors and these were found to agree quite well with

those obtained from magnetoacoustic measurements. No other sheet of the magnesium Fermi surface, however, satisfies the inversion criteria and for these one must rely on area calculations based on some simple Fermi surface models. One generally assumes that the model is valid if the calculated cross-sectional area branches agree reasonably well with experimental data. The problem with most model calculations, however, is that this process is by no means unique. The best model calculations for simple metals, i.e., those with tightly bound inert-gas-like cores, seems to be those based on the pseudopotential model Hamiltonian.

The DHVA data reported here contain nearly complete information on all sheets of the Fermi surface except the small first-band cap. If we describe the area branches in terms of solid angles of **k** vectors at the Fermi surface, this data covers over 90% of the total Fermi surface. In the following paper, we will use this data together with that presented in I to obtain Fermi surface models using the pseudopotential approximation for the band structure. For this reason we have made no attempt in this paper to obtain quantitative agreement with any simple model. We note, however, that qualitatively the data are in excellent agreement with the predictions of the single-OPW model[2] and had we made the comparison, we would have found that the two-OPW model[1] also gave reasonable quantitative agreement.

The Fermi Surface of Magnesium III: Local and Nonlocal Pseudopotential Band Structure Models for Magnesium*

J. C. Kimball† and R. W. Stark‡

Department of Physics and James Franck Institute, The University of Chicago, Chicago, Illinois

AND

F. M. Mueller

Argonne National Laboratory, Argonne, Illinois

(Received 17 April 1967)

Extensive de Haas–van Alphen cross-sectional areas and magnetoacoustic calipers for the magnesium Fermi surface were used to generate local- and nonlocal-pseudopotential model Hamiltonians. Both models yielded a good representation of the Fermi surface. Small but significant deviations from experimental data could not be eliminated using the local model, but these were eliminated with the nonlocal model. The values of the local-pseudopotential Fourier coefficients obtained were $U_{10\bar{1}0} = +0.014$ Ry, $U_{0002} = +0.026$ Ry, $U_{10\bar{1}1} = +0.036$ Ry, and $U_{10\bar{1}2} = +0.058$ Ry. The variational parameters for the nonlocal pseudopotential were the Fourier coefficients of the self-consistent ion-core potential $V(r)$. The values obtained for these were $V_{10\bar{1}0} = -0.440$ Ry, $V_{0002} = -0.412$ Ry, $V_{10\bar{1}1} = -0.386$ Ry, and $V_{10\bar{1}2} = -0.299$ Ry.

INTRODUCTION

THIS paper is the third in a series devoted to the experimental and theoretical determination of the band structure of magnesium. The first paper[1] in this series, which will henceforth be referred to as I, dealt with extensive magnetoacoustic investigations; the second paper,[2] henceforth to be referred to as II, described the results of extensive de Haas–van Alphen investigations. In general, the data contained in I and II have been found to be in *qualitative* agreement with the single-OPW model[3] and Falicov's first principles OPW calculations (OPW = orthogonalized plane wave).[4]

The agreement with Falicov's model is in fact within his estimated error of about 5% of the Fermi energy E_F; the principal part of this error results from uncertainties in the electron correlation and exchange energies. The available experimental data is sensitive to variations of about 0.1% in E_F; current first-principles calculations can not approach this accuracy. Thus, in order to take full advantage of these data (which are limited to the energy contour E_F) in gaining insight into the magnesium band structure, one must use a semiempirical model Hamiltonian such as those based on pseudopotential theory.[5,6]

This approach has the dual advantage of acting as an interpolation procedure whereby limited experimental information can be used to generate the entire Fermi surface, and of generating $E(\mathbf{k})$ bands for $E(\mathbf{k}) \neq E_F$.

[1] J. B. Ketterson and R. W. Stark, Phys. Rev. **156**, 748 (1967).

[2] R. W. Stark, Phys. Rev. (preceding article).

[3] W. A. Harrison, Phys. Rev. **118**, 1190 (1960).

[4] L. M. Falicov, Phil. Trans. **A255**, 55 (1962).

[5] W. A. Harrison, *Pseudopotentials in the Theory of Metals* (W. A. Benjamin, Inc., 1966), and enclosed references.

[6] J. M. Ziman, Advan. Phys. **13**, 89 (1964).